**RESEARCH OUTPUTS / RÉSULTATS DE RECHERCHE**

# Correlation of structural and optical properties using virtual materials analysis

Moskovkin, Pavel; Badorreck, Holger; Steinecke, Morten; Jensen, Lars; Ristau, Detlev; Jupe, Marco; Muller, Jérôme; Lucas, Stéphane; Pflug, Andreas; Grineviit, Lina; Selskis, Algirdas; Tolenis, Tomas

[Link to publication](Link to publication)

*Citation for pulished version (HARVARD):*
Moskovkin, P, Badorreck, H, Steinecke, M, Jensen, L, Ristau, D, Jupe, M, Muller, J, Lucas, S, Pflug, A, Grineviit, L, Selskis, A & Tolenis, T 2019, 'Correlation of structural and optical properties using virtual materials analysis', *Optics Express*, vol. 27, no. 16, pp. 22209-22225. https://doi.org/10.1364/OE.27.022209

# Correlation of structural and optical properties using virtual materials analysis

**Holger Badorreck,**[1,*] **Morten Steinecke,**[1] **Lars Jensen,**[1] **Detlev Ristau,**[1] **Marco Jupé,**[1] **Jérôme Müller,**[2] **Romain Tonneau,**[2] **Pavel Moskovkin,**[2] **Stephane Lucas,**[2] **Andreas Pflug,**[3] **Lina Grinevičiūtė,**[4] **Algirdas Selskis,**[4] **and Tomas Tolenis**[4]

[1]*Laser Zentrum Hannover e.V.,Hollerithallee 8, Hanover, Germany*
[2]*University of Namur, rue de Bruxelles 61, Namur, Belgium*
[3]*Fraunhofer-Institut für Schicht- und Oberflächentechnik (IST), Bienroder Weg 54 E, Braunschweig, Germany*
[4]*Center for Physical Sciences and Technology, Savanorių Ave. 231, Vilnius, Lithuania*
[*]*h.badorreck@lzh.de*

**Abstract:** Thin film growth of $TiO_2$ by physical vapor deposition processes is simulated in the Virtual Coater framework resulting in virtual thin films. The simulations are carried out for artificial, simplified deposition conditions as well as for conditions representing a real coating process. The study focuses on porous films which exhibit a significant anisotropy regarding the atomistic structure and consequently, to the index of refraction. A method how to determine the effective anisotropic index of refraction of virtual thin films by the effective medium theory is developed. The simulation applies both, classical molecular dynamics as well as kinetic Monte Carlo calculations, and finally the properties of the virtual films are compared to experimentally grown films especially analyzing the birefringence in the evaluation.

## 1. Introduction

In recent years, the Virtual Coater (TM of the University of Namur) approach was developed to establish a complete theoretical model of physical vapor deposition [1,2]. The concept is based on the combination of different simulation techniques forming a powerful multiple scale model. Each particular simulation method is chosen precisely according to the specific physical process. The Virtual Coater covers the material transport in the coating chamber, the atomistic thin film growth and the calculation of electronic and optical properties. For the transport simulation the Boltzmann transport Eqs. for a multiple body problem are solved by the Direct Simulation Monte Carlo (DSMC) method. This simulation delivers the physical movement and interaction of the atoms at the substrate, which can be used for the atomistic growth simulation. Alternatively, discrete energies and a specific angle of incidence can be investigated for a more fundamental analysis, which does not address a certain coating machine. Classical molecular dynamics (MD) simulations for the virtual thin film growth [1,3–5] deliver the structural properties, however they are limited in structure size. Alternatively, the kinetic Monte Carlo (kMC) approach for the atomistic growth can handle much larger structures reaching realistic thin film thicknesses. kMC is widely used for the description of particle deposition processes and film growth as well as for others processes in nanoscale systems, for reference see the review [6]. The model used in this work is described in detail in [2,7,8] and below a brief description of the model is given. The influence of the structure size and the simplification of the atomistic structure are still not investigated in detail. By comparison of both techniques with each other and with experimental coatings a detailed analysis of the validity and applicability of the simulation methods can be

performed. However dependent on the growth conditions, the coatings vary regarding their nanostructure, mass density, stoichiometry, or surface roughness [9]. Consequently, different optical and electronic properties are achieved. Ab-initio calculations can deliver these properties applying the density functional theory (DFT) and the Kramers-Kronig relation. With respect to the state of the art computational power and the algorithm complexity of the DFT of $\approx O(n^3)$, the manageable structure sizes are limited to a so-called super-cell including about 100 atoms [10]. If this small volume represents the structure well, e.g. densely packed bulk materials, the ab-initio calculations are able to provide the optical properties. Solving the quantum mechanical multiple body problem of the respective super-cell, the main input parameters are the mass density and the stoichiometry. Regarding the applied coating processes, typical materials do not fit the requirements for the DFT simulation. For porous materials or structures with a low packing density and imperfections like voids, the optical properties typically cannot be obtained by a single DFT approach. Only if the inhomogeneities are in the dimension of the atomistic structure of the super-cell, the DFT approach delivers physically reasonable values, which allows calculating the behavior of amorphous solids [10] The effective medium theory offers an effective solution to also incorporate nano- to microscopic structural inhomogeneities. Optical properties of porous or mixed materials (compounds like $TiO_2$ are treated as a single material) can be calculated by the combination of the optical properties of each single, dense material, as well as the vacuum properties of the voids. The amount of the different materials does not influence the physical properties solely, also their internal structure has an impact. Since pores are generally not radially symmetric, the anisotropic effective medium theory is considered here. Consequently, both models allow describing the material characteristics in a specific range. The DFT addresses dense and homogeneous materials and the effective medium theory implements the structural properties. The combination of both methods provides the possibility to study how the index of refraction depends on the material structure in a more general way. In the presented paper the structural properties of $TiO_2$ thin films as well as their influence on the index of refraction are theoretically and experimentally investigated and the validity of the proposed models is discussed. For the theoretical description a novel algorithm implementing both, the pure material index of refraction as well as the influence of the nanostructure of the film is developed. On the basis of the Virtual Coater concept, the $TiO_2$ single layer film growth by electron beam evaporation as well as by DC reactive magnetron sputtering is simulated by means of MD as well as kMC. The results of both theoretical approaches are compared to each other, and to the experimental findings.

## 2. Combination of structural and bulk optical properties by effective medium approximation

Experimentally, the electronic and optical properties of dielectric materials are related to the manufacturing processes. Generally, it has to be differentiated between two structural types: Dense structures without voids, and nanostructured materials including columns or voids. The model based synthesis of virtual films can describe both types, but a sufficient determination according to the quantum mechanical approach can only be achieved for dense structures. With respect to the limited super-cell size, the quantum mechanical calculation cannot handle structures with inhomogeneities like voids or pores. Nevertheless, one can approximate optical properties of porous films by associating their structure to homogeneous materials of the same mass density, and neglecting the structural properties, like the uniformity of their structure [1]. However, the implementation of the structural properties will improve the simulated result by combining the structural properties obtained from the atomistic growth and the optical properties of dense bulk materials. With the Bruggeman effective medium approximation [11–13], there is an established theory, which even allows to calculate anisotropic optical properties from the structural information and bulk optical properties. The general approach is as follows. First, the

pore distribution in the film structure has to be determined. For this purpose, a three dimensional
Cartesian grid is utilized which defines the space that is filled with material (grid cell contains
atoms), and the space of the voids (grid cell contains no atoms), in a more useful way for further
processing. The cell dimension should be equal or larger than the length of the atomic bonds,
otherwise interatomic positions are mistakenly recognized as voids or for much larger cell sizes
small pores are not covered correctly. The resulting pore statistics allow applying the Bruggeman
effective medium approximation which is described by

$$\sum_{n}^{m} f_n \frac{\epsilon_n - \epsilon^{\text{eff}}}{\epsilon_n + 2\epsilon^{\text{eff}}} = 0 \tag{1}$$

resulting in the effective permittivity $\epsilon^{\text{eff}}$ by the mixing of m materials with their amount $f_n$ and
permittivity $\epsilon_n$. Using the Maxwell relation $n^2 = \epsilon^{\text{eff}}$, the effective refractive index of a structure
containing voids can be computed. If only 2 materials (including voids) are considered, Eq. (1)
can be solved analytically. Then, only the physical reasonable solution has to be selected. For
more materials this analytical solution cannot be applied but numerical methods are available
[14]. To handle also anisotropic effective medium effects, the more generalized form of the Eq.
known as "traditional anisotropic Bruggeman effective medium theory" (TAB-EMA) is utilized
[11]:

$$\sum_{n}^{m} f_n \frac{\epsilon_n - \epsilon_j^{\text{eff}}}{\epsilon_j^{\text{eff}} + L_j \cdot (\epsilon_n - \epsilon_j^{\text{eff}})} = 0 \tag{2}$$

The Eq. involves the depolarizing factors

$$L_j = \frac{U_x U_y U_z}{2} \int_0^{\infty} 1 / \left[ (s + U_j^2) \sqrt{(s + U_x^2)(s + U_y^2)(s + U_z^2)} \right] ds \tag{3}$$

which are based on the potential of uniformly polarized ellipsoids and only depend on the ellipsoid
shape parameters $U_j$, with j = x, y, z. To obtain representative ellipsoid shape parameters for
a given atomistic structure, the structure tensor S is determined by the integral of the material
gradients [15], which is exchanged by the sum for the numerical investigation:

$$S = \int \begin{pmatrix} (\nabla_x \rho)^2 & \nabla_x \rho \nabla_y \rho & \nabla_x \rho \nabla_z \rho \\ \nabla_y \rho \nabla_x \rho & (\nabla_y \rho)^2 & \nabla_y \rho \nabla_z \rho \\ \nabla_z \rho \nabla_x \rho & \nabla_y \rho \nabla_z \rho & (\nabla_z \rho)^2 \end{pmatrix} \partial r = \sum_r \begin{pmatrix} (\nabla_x \rho)^2 & \nabla_x \rho \nabla_y \rho & \nabla_x \rho \nabla_z \rho \\ \nabla_y \rho \nabla_x \rho & (\nabla_y \rho)^2 & \nabla_y \rho \nabla_z \rho \\ \nabla_z \rho \nabla_x \rho & \nabla_y \rho \nabla_z \rho & (\nabla_z \rho)^2 \end{pmatrix}, \text{with } \rho = \rho(r) \tag{4}$$

To keep the calculation fast and simple, for the density $\rho$ the pore distribution represented by the
Cartesian grid as described above is used. The structure tensor is computed in each point and
is cumulated by the sum to an effective structure tensor describing the full structure. For the
calculation of the density gradients second order accurate central differences are used and the
structure tensor is then diagonalized by singular value decomposition. This results in the three
principal components and the associated rotation matrix R. The components $S_j$ correspond to the
inverse ellipsoid shape $U_j$.

$$S = R \begin{pmatrix} S_x & 0 & 0 \\ 0 & S_y & 0 \\ 0 & 0 & S_z \end{pmatrix} R^T = R \begin{pmatrix} 1/U_x & 0 & 0 \\ 0 & 1/U_y & 0 \\ 0 & 0 & 1/U_z \end{pmatrix} R^T \tag{5}$$

The inverse behavior of the main components is due to the small gradient in the direction of
elongated ellipsoids, whereas the gradient is high in perpendicular direction. With the ellipsoid

shape parameters $U_j$ and the material amounts $f_n$ the anisotropic effective permittivity can be calculated by Eqs. (2) and (3). For the following analysis of the MD structures, a grid resolution of 2 Å is chosen, which is at the lower bound of the useful range. For this value in a dense structure with its usual atomic distances of $TiO_2$ a falsely pore detection is avoided. Further, to prevent an overrated effect of the surface or substrate region, the analysis is constrained to a range with a low variance of the mean density in growth direction. This is motivated by the fact, that the thicknesses of the simulated structures are about one magnitude smaller compared with the experimental structures. To exclude these regions at the top and the bottom, the mean density is determined for each atomic grid layer and layers with a deviation larger than 10% of the median of these mean densities are discarded.

## 3. Virtual coater methods

In the following the methods used in the Virtual Coater concept are described. The Virtual Coater concept is a flexible multiple scale approach combining different simulation techniques to produce a virtual material. This material is a digital blue print of the real material for a specific coating process. The material transport from the source to the target through the gas phase or plasma, the atomistic nucleation at the substrate and the determination of the material properties are simulated in specific, numerical calculations which are linked by well-defined software interfaces [1]. For the material transport the Direct Simulation Monte Carlo (DSMC) or Particle in Cell Monte Carlo (PIC-MC) method is often applied. [16,17]. State of the art software solutions allow implementing specific designs of the coaters and the physical processes inside them. A detailed insight is provided by the literature [18] and the example of a DC magnetron plant, which is discussed in the following. For the atomistic growth simulation, two different methods are applied in this investigation. Both methods, MD and kMC, are described in the subsections. For the evaluation of the structural and optical properties, both, classical and ab-initio methods are applied. For the ab-initio method DFT [19–21] applying the hybrid functional HSE06 [22] size is computationally limited to about 100 atoms. For a more detailed description, how this method is applied in the Virtual Coater framework, see [10]. Generally, the concept provides a full description of the coating process allowing studying the effects of different parameters of the process on the film structure and its properties. For this investigation the atomistic simulation is essential for a precise reproduction of the structural properties in the virtual material. Consequently, the MD and the kMC are introduced in the next sections in more detail.

### 3.1. Atomistic thin film growth - molecular dynamics (MD)

For the growth calculation of $TiO_2$ films, the well-established Matsui interaction potential [23] is used for the classical molecular dynamics (MD) simulations, where the calculation of the atomic movement is performed by the software DL_POLY [24]. For the growth simulation two dimensional boundary conditions are necessary achieving a surface of the solid, and in addition the summation according to Wolf et al. has to be applied to generate a realistic structure, which can also show differences from the perfect stoichiometry [25]. For the simulation some numerical approximations are necessary to provide practical realistic structure sizes. Both, the temporal simplification as well as the spatial limitation of the structure were proven by numerous studies. The impact of the atom is calculated in two steps. The impact of the adatom is calculated at constant total energy of the atomistic system according to NVE (constant number of particles N, constant volume V, and constant energy E). The number of steps is calculated by the software and can vary between 200 and 1000 integrations. In the second step, the structure is cooled down to a defined structure temperature by the Anderson thermostat in a NVT step [26]. The development time of a single event is about 1ps, while the integration time step is 2fs. Consequently, the simulation cannot calculate the same development time like in an experimental deposition event,

especially diffusion is neglected. For the deposition of a single atom a small volume of $3 \times 3 \times 4$ nm$^3$ is extracted from the original structure around the centered position of the impact point of the adatom, respectively. For the estimation of the interaction zone, both lateral directions in the surface plane as well as the depth are investigated. The interaction zone in the subsequent simulations is defined as the region in the Titania structure which is effectively modified by the bombardment of the particle. In Fig. 1, the displacement of the atoms for 1000 impacts is presented. The area of $3 \times 3 \times 4$ nm$^3$ covers 99.5 percent of the atomic displacements which is sufficient for a reasonable simulation. In particular, this procedure requires the extraction of a corresponding cell out of the total structure, the supply of this cell to a MD simulation for deposition event modeling and subsequently, the reassembly into the total ensemble. To ensure that the assembly of the simulation cell into the total system is not resulting in outsized accelerations due to small distances between the atoms at the cell border, the simulation cell is extended by a region of frozen atoms (Fig. 1). The thickness of this region, which surrounds the simulation cell, is 8.1 Å in each direction. The involved atoms inside this region are additionally extracted from the total system. Due to this procedure, uncontrolled acceleration can be excluded when the simulation cell is reinserted after the deposition event modeling.
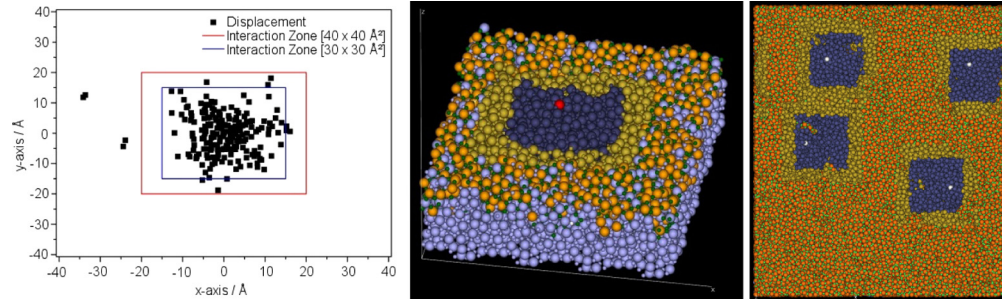


**Fig. 1.** Left: Investigation of the impact volume; lateral position (x,y) at 0.8 ps system development time, which corresponds approximately to the NVE simulation time in the deposition event modeling. Middle: 3D view of the selected cell around the impact point; mobile atoms (blue), frozen atoms (yellow), titanium atoms (orange), oxygen atoms (green), substrate atoms (light blue), and impinging atom (red). Right: Parallelization of the deposition process, blue ranges mark the position of the deposition of the atoms

Additionally, a minimum number of 3000 atoms in the extracted simulation cell is ensured. In the case that the number of atoms is not reached, the depth of the box is increased until the set value is achieved. The gain in time by application of this approximation rises with the number of atoms deposited on the substrate. This results from the fact that the ratio of atoms involved in the MD simulation, compared to the size of the complete structure, decreases with growing layer thickness. Finally, the presented model approach is used to simulate thin film growth with up to $10^5 - 10^6$ deposited atoms using the computational power of a state of the art personal computer. Experimentally, the probability of a deposition of more than one atom in the temporal frame and in the interaction area is negligible which eventually leads to a sequential deposition in the growth simulation. This sequential deposition reduces the deposition speed in the simulation and limits the speed benefit of parallelization. Nevertheless, the implementation of GPU computing promises a reduced simulation time by a factor of about five. Additionally, the calculation speed can be increased by deposition of several atoms at the same time. In this procedure, the algorithm generates independent deposition events without overlaps of the calculation cells. In this case the events can be computed in parallel with increased growth rates depending on the structure size. As a consequence, the capacity of high performance computers can be utilized much better.

Figure 1 displays the procedure which is realized in the self-developed "Pluto" software that controls the MD-growth simulation.

### 3.2.　Atomistic thin film growth - kinetic Monte Carlo (kMC)

Kinetic Monte Carlo simulations are performed by using the NASCAM software package [27], which is described in detail in [2,8]. For the glancing angle deposition of titanium dioxide, Ti and O atoms are considered to be randomly thrown towards the substrate with velocities according to energy and incident angular distribution functions. These distributions are the output of the transport simulations and they are used as input for the film growth simulations. Deposited particles may occupy predefined atomic positions in a lattice. A simple cubic lattice is used. Such a lattice may be used as a model for the amorphous state of $TiO_2$ since no difference on the crystallographic configuration is made in this work. The flux of each species is characterized by its own energy and angular distribution of incident atoms. The ratio of the flux intensities is important and determines the stoichiometry of the film [2]. The intensity of the oxygen flux to the substrate may be calculated from the kinetic gas theory; it depends on the partial oxygen pressure in the discharge chamber and the temperature. The intensity of the Ti incident flux may be estimated from the film growth rate. If the growth rate is unknown, one can estimate the flux on the base of the sputtering yield of the target, discharge current and the ratio of sputtered to condensed Ti atoms. The last ratio can be obtained from the transport simulations. The sticking coefficient for Ti is assumed to be 1, whereas the sticking coefficient for oxygen depends on the local stoichiometry of the growing film. If the local stoichiometry of the film within the search radius $L_d$ is less than 2, an oxygen atom is assumed to attach to the film. Otherwise, it is reflected. The search radius is equal to 2 interatomic distances in the presented work. This sticking model mimics the possible short diffusion of oxygen at the film [28]. As the sticking coefficient of oxygen is less than 1, the incident flux of oxygen is much higher than the incident flux of titanium. In the present study in order to have a stoichiometric oxide the intensity of the incident flux of oxygen is set to be 100 times higher than that of titanium. The parameters of the simulations are summarized in Table 1. In the simulations the energy transfer from the incident atoms to the film is taken into account. It is supposed that the incident atoms transfer a part of their energy to a primary recoil and to their nearest neighbors. The value of the transferred energy is calculated on a basis of binary collision approximation and depends on the value of the impact parameter of the collision. The last is chosen randomly in the range from 0 to an atomic diameter.

**Table 1. NASCAM simulation parameters used for this study.**

| Parameter | Values |
|---|---|
| Substrate size (nm) | $30 \times 30$ |
| Total number of deposited atoms, Ti and O | $1 \times 10^6$ |
| Oxygen to titanium incident flux ratio | 100 |

## 4.　Application to atomistic structures

The theoretical description of the refractive index requires the knowledge of the nanostructure of the thin film. Generally, the nanostructures of dielectric layers are related to the coating process and to the individual deposition plant. As already known, e.g. from glancing angle deposition (GLAD) coatings, the structure of the thin film depends on the angle of incidence and on the kinetic energy of the deposited atoms, e.g. see [2]. It has to be mentioned that the kinetic energy of depositing atoms depends on the generation process and also on the conditions in the reactor. For example, the energy can be reduced by interatomic collisions during the propagation from the material source to the substrate. That leads to thermalization of the atoms

and molecules, which has a significant influence on the nanostructure. As a consequence, it is useful to perform simplified as well as complete simulations, applying the full simulation framework. Here, simplified simulations mean that the atomistic simulations are performed using discrete deposition energies of 0.1eV, 1eV and 10eV for a perpendicular angle of incidence (0°) and for the energy of 0.1eV for the different angles of incidence of 0°, 30°, 50° and 70°, respectively. For comparison with experimentally obtained refractive index values, coatings grown by electron beam evaporation under the defined deposition angles are considered, because the particle energy for thermal evaporation is in the range of 0.1eV. For the "Mantis"-coater of the University of Namur featuring a DC magnetron process, the complete simulation based on the full Virtual Coater concept is performed. This coating plant exhibit two targets with a distance of about 15cm to the substrate and with a working pressure of 0.5 Pa. For a detailed description of the coating plant and the transport simulations, including all relevant parameters of the construction and geometric characteristics, see Ref. [2].

In the first step, the material emission of magnetrons and its transport through the discharge chamber are calculated using PIC-MC simulations. The final output of these simulations are the angular and energy distributions at the substrate [16,17]. In the configuration of the coating plant, the kinetic energy of the sputtered titanium atoms is mainly thermalized which leads to a Boltzmann like energy distribution of the adatoms. In addition, compared to the amount of titanium, about 1% of high energetic oxygen atoms is included in the simulation. These parameters are used as an input for the atomistic simulation of the film growth. For the simulation two different cases are investigated. As shown in Fig. 2, in the first case the tilt angle is kept constant at zero degree and with respect to the symmetry of both magnetrons with an azimuthal angle of ±45°; the average particle flux can be approximated to be normal. In the second case the tilt angle of incidence is in the glancing configuration. However, the transport simulation delivers the input parameters as particle energy and angular distribution for the growth simulation.
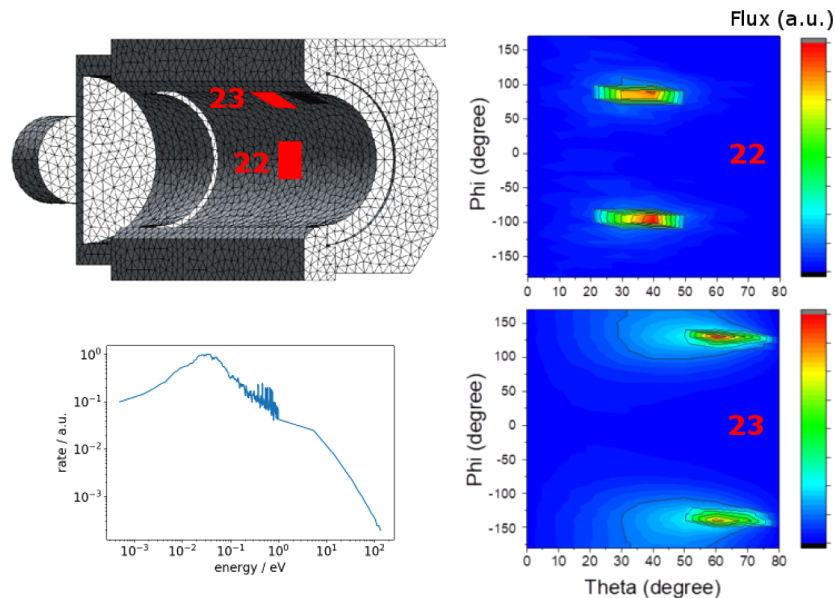


**Fig. 2.** Substrate positions in the substrate holder of the "Mantis"-coater with histograms of the energy and angular distribution functions of the incident titanium atoms. The oxygen distribution is highly thermalized compared to the titanium distribution (see also Ref. [2]).

### 4.1. Molecular dynamics - discrete conditions

In the following the investigations of the structural properties using MD simulations are presented. In this study the simplified approach of discrete kinetic energies of the incident atoms and angles of incidence (AOI) is applied. The structural development with varying kinetic energy and normal incidence of the atoms is illustrated in Fig. 3, where structures grown at a substrate with the footprint size of $7 \times 8 nm^2$ are presented with their density profiles in growth direction. Under typical evaporation conditions with a deposition energy of $E_{kin} = 0.1$ eV, the structure starts with an initial density of 4.25 g/cm$^3$, which is related to the density of the substrate structure consisting of the same material. The fast drop to smaller densities at about 3.0 g/cm$^3$ is caused by the porous structure that is displayed by the cross-sections of the atomistic structure. For a growth using deposition energies of $E_{kin}$= 1eV, the drop in mass density is significantly lower with a value of 3.9g/cm$^3$ at the layer surface. Consequently, the atomistic structure exhibits only a few small pores. The third structure deposited at $E_{kin}$=10eV shows no change in the mass density with 4.2 g/cm$^3$ and a densely packed atomic structure. The fluctuations are mainly related to numerical variations due to the structural size. The smaller initial density here is caused by the high deposition energy, which has an impact also on the substrate structure below the first atomic layer surface and results in a slight relaxation of the substrate structure.
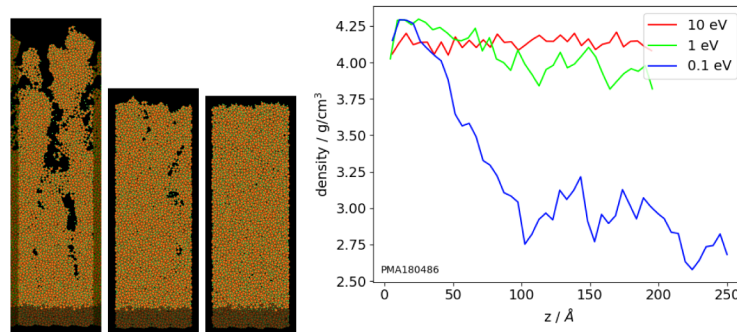


**Fig. 3.** Atomistic structures grown by MD with deposition energies of 0.1eV, 1eV and 10eV from left to right. The atoms are deposited on a substrate with a footprint size of 7×8nm$^2$ (bottom shaded part). Each structure contains 100k atoms; the growth takes place at the top. Shown are 12 Å thick cross sections in the paper plane. On the right, the density profiles in growth direction are plotted, which show a correlation between deposition energy and density.

Consequently, utilizing Eq. (1), a resulting effective refractive index dependent on z can be computed; the refractive index is closely related to the density distribution and shows the same behavior. This is especially true for structures grown at low deposition energies. In this case, the refractive index changes over the growth direction according to the large density variations.

However, the full index of refraction ellipsoid for a more complete description of the anisotropy is preferable. The clear orientation of the pores in growth direction results in an anisotropy compared to the lateral directions. A possible random anisotropy in the lateral directions however is mainly related to the small structure size, here. In Fig. 4 on the left, the ellipsoid represents the pore shape and orientation calculated according to Eq. (4) for the structure grown at 0.1eV. The effective refractive index ellipsoid obtained by utilizing this pore ellipsoid shape and Eq. (2) for an exemplarily bulk refractive index of 2.3 at 1000nm is displayed on the right. The principal axis is slightly tilted and exhibits a pronounced anisotropy in the growth direction z as the prominent direction. The calculated direction dependent refractive index varies between 1.82 and 1.97. It is worth to mention, that the deposition angle has a high impact on the structures grown by PVD processes. For high surface roughness, which especially occurs for low deposition

energies, shadowing effects cause a self-amplification that lead eventually to a columnar growth. In Fig. 5 structures grown at 0.1eV deposition energy with different incident angles of 0°, 30°, 50° and 70° are compared. The cross sections of the structures illustrate the slanted columnar growth which is also indicated by each representing pore ellipsoid at the bottom. While the structure for 0° shows a stochastic-like pore distribution, a superordinate orientation of single pores for 30° can be suggested. For 50° the pores are more connected and for 70° a full columnar structure is obtained. A small drop of the density of the columns from 4.27 to 4.08 g/cm$^3$ is observed. However, this is in the range of the grid discretization error and therefore not further discussed. The mean density of the full structure drops significantly from 2.95 to 1.95 g/cm$^3$ and the fill factors can be calculated by the division of these two values. The values of the pore ellipsoid angle and the main components of the resulting effective index ellipsoid are given in Table 2. The incident angle determines the growth angle of the columns, and larger incident angles result in larger column tilting angles, but for a determination of a clear correlation further studies are necessary. For normal incidence a columnar angle of 0° can be expected, so we get a rough estimate of the variance due to stochastic processes in the relation between incident and columnar tilting angle. The structures show slanted columns with tilting angles $\sigma$, that correlate well, while giving slightly smaller values, with the values resulting from the empirical tangent rule $\tan \sigma = 0.5 \tan \theta$ [29] (16° for 30°, 31° for 50°, 54° for 70°). The resulting refractive indices exhibit a large anisotropy which continuously grows with the deposition angle. For 0° the anisotropy is about 8%, for 30° it is 9%, 50° exhibits an anisotropy of more than 13%, and 70° results in about 22% between the different directions of the refractive index. However, the small structural size especially in the lateral directions can introduce inaccuracies, e.g. the anisotropy can be overestimated due to stochastic effects.
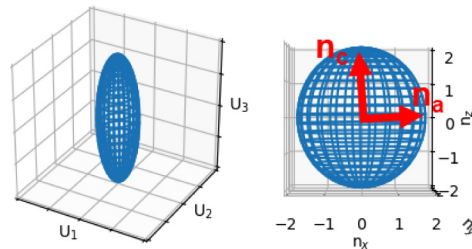


**Fig. 4.** Left: Ellipsoid representing the pore shape and orientation (i.e. the inverse structure tensor $U_j$ from Eq. (4) and (5)) for the structure grown with 0.1eV. Right: resulting refractive index ellipsoid for an index of refraction of the dense material of n=2.3, oriented like in the structure. The main components, indicated by red arrows, vary within 1.82 and 1.97. (calculated by Eq. (2))

### 4.2. Kinetic Monte Carlo - discrete conditions

The kMC is a flexible and fast method for the determination of atomistic structures. The kinematic approach of the kMC reduces the calculation time compared to the MD simulation and facilitates the generation of structures with 1 Million atoms in a 2-3 orders of magnitude faster simulation process. This advantage is at the expense of flexibility of the atomistic movements of atoms and a different description of the interactions between the atoms. Consequently, a comparison of kMC and MD structures seems to be desirable. However, in the low energy regime, where the particle energy is below the displacement threshold for atoms at the surface of 3eV, atoms once deposited are not moving at the surface. Figure 6 shows the structures as cross sections consisting of four atomic layers (correspondent to about 10Å) for deposition angles of $\theta = 0°$, 30°, 50° and 70° from left to right. Below each structure the resulting pore ellipsoid is shown, which reproduces
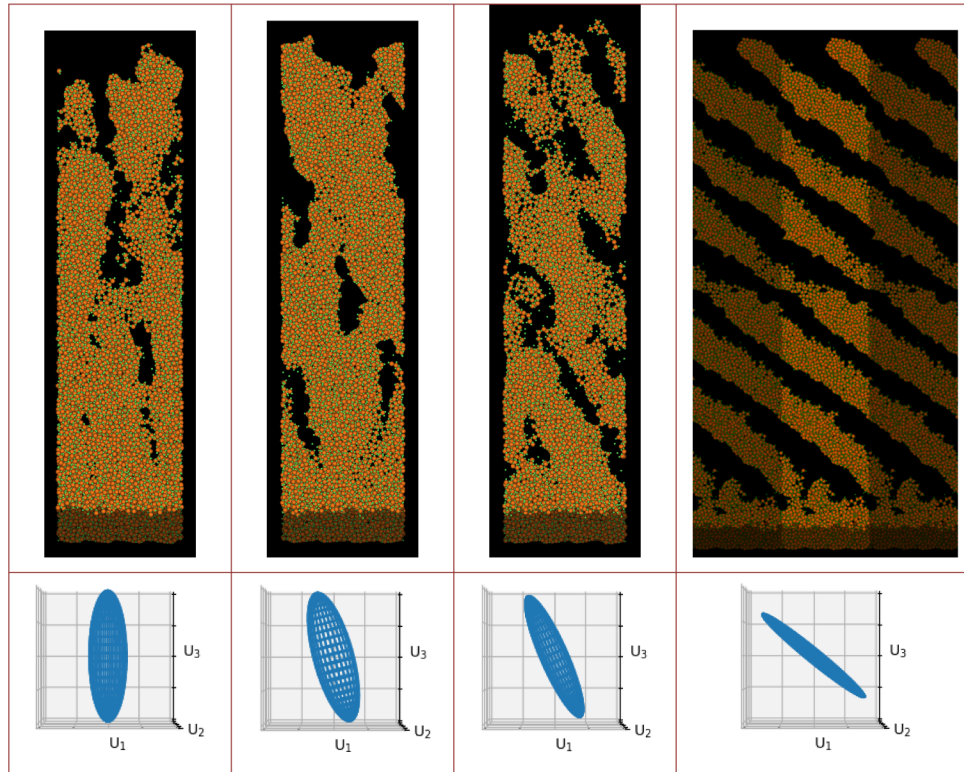
**Fig. 5.** Structures containing 100k atoms grown with the molecular dynamics method at a deposition energy of 0.1 eV under different deposition angles, from left to right: 0°, 30°, 50° and 70°, also indicated by the arrows. For 70°, also the periodic continuation is viewed as shaded structure. The cross sections analog to Fig. 3 illustrate well the porous structure. The subfigures in the bottom row show the pore ellipsoids for each structure, by which the main direction of the columnar structure is well reproduced.

**Table 2.** The resulting pore ellipsoid angles and main components of the refractive index ellipsoid (for an assumed bulk refractive index of 2.3) of the structures grown by molecular dynamics shown in Fig. 5.

| deposition angle $\theta$ | mean density (full structure) (g/cm$^3$) | density of columns (g/cm$^3$) | angle of pore ellipsoid $\sigma$ | main components of refractive index ellipsoid | | |
|---|---|---|---|---|---|---|
| 0° | 2.95 | 4.27 | 0° | 1.820 | 1.843 | 1.967 |
| 30° | 2.90 | 4.18 | 15° | 1.803 | 1.859 | 1.968 |
| 50° | 2.53 | 4.18 | 24° | 1.650 | 1.736 | 1.874 |
| 70° | 1.95 | 4.08 | 51° | 1.423 | 1.655 | 1.736 |

well the main direction of the columnar structure. For a deposition angle of 30°, the resulting pore ellipsoid angle is in the same range as the value obtained for normal deposition angle (0°). This could be explained by the fact, that the structure exhibits pores, but these pores are not large enough to form a columnar structure by shadowing effects as is also proposed by the cross section depicted in Fig. 6. However, the tangent rule is roughly reproduced for a deposition angle of 50° and 70°. For an assumed bulk index of refraction of 2.3, the resulting main components of the index ellipsoid are given in Table 3. The table shows the resulting anisotropy of the kMC structures, which are 1% for 0°, 3% for 30°, about 5% for 50°, and 11% for 70°, respectively. The mean densities and the fill factors, respectively, give higher values for the kMC structures compared with MD (see Tables 2 and 3). Therefore also the resulting indices of refraction are larger for the kMC.
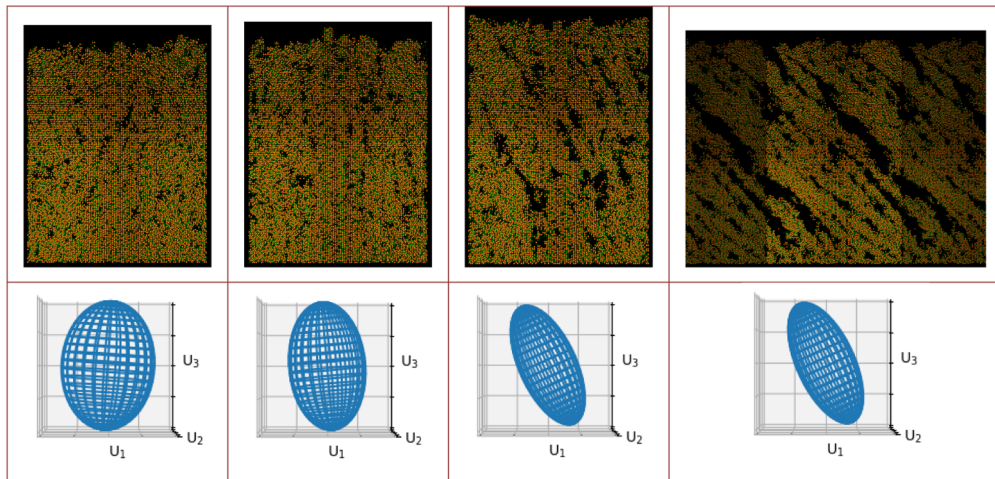


**Fig. 6.** Structures with 1 Mio. atoms grown with the kinetic Monte Carlo method (cuts of 4 atomic layers, ≈ 10 Å) under different deposition angles, from left to right: 0°, 30°, 50° and 70°, as indicated by the arrows. For 70°, also the periodic boundary conditions are viewed by the shaded structure. The subfigures in the bottom row show the pore ellipsoids for each structure, which correspond well with the main direction of the columnar structure.

**Table 3. The angle of the pore ellipsoid and the main components of the refractive index ellipsoid (for a bulk refractive index of 2.3) of the kMC simulations shown in Fig. 6.**

| deposition angle $\theta$ | fill factor | angle of pore ellipsoid $\sigma$ | main components of refractive index ellipsoid | | |
|:---:|:---:|:---:|:---:|:---:|:---:|
| 0° | 85% | 4° | 2.078 | 2.082 | 2.108 |
| 30° | 80% | 5° | 2.008 | 2.015 | 2.060 |
| 50° | 75% | 24° | 1.913 | 1.936 | 2.009 |
| 70° | 61% | 44° | 1.680 | 1.733 | 1.870 |

## 5. Experimental coatings and their analysis

For the experimental verification of the virtual materials, both, a GLAD e-beam based coating plant at the Center for Physical Sciences and Technology as well as the Mantis coater from the University of Namur were employed. For the determination of the refractive index tensor of the materials a few brief theoretical definitions and descriptions are given.

For normal light incidence on experimentally grown samples, two refractive indices can be measured for the perpendicular light polarizations. The different light polarizations are defined here as s-polarized light, which is normal to the plane defined by the surface normal and the columnar direction, while p-polarized light is parallel to that plane. As described in [30] with s-polarized light, one main component ($n_b$) can be measured, while with p-polarized light ($n_{||}$), a combination of $n_a$ and $n_c$ is measured, with $\sigma$ being the angle between the light and the direction of the columns ($n_c$):

$$n_{||} = \sqrt{\frac{n_a^2 n_c^2}{n_c^2 \cos^2(\sigma) + n_a^2 \sin^2(\sigma)}} \tag{6}$$

The series of experimentally grown structures was manufactured by the e-beam evaporation plant VTD VERA1100 equipped with GLAD system (see Fig. 7), where the distance between source and substrate was 33 cm. The deposition rate was maintained at 3 Å/s and controlled with a quartz crystal monitor. Four samples were fabricated by changing the deposition angle between the substrate normal and vapour flux in following values: 0°, 30°, 50°, 70°. To ensure the oxidation of evaporated titania, a reactive process with oxygen flow was employed. All processes were started at a vacuum pressure of $1.5 \times 10^{-5}$ mbar, and the oxygen gas was introduced into the chamber to keep the pressure at $2.0 \times 10^{-4}$ mbar constant during the evaporation.
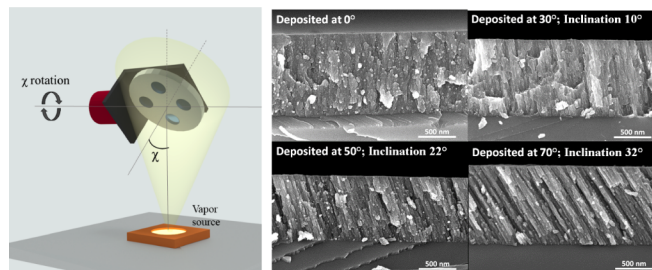


**Fig. 7.** Left: The principal scheme of glancing angle deposition, with the angle $\chi$ between the vapor flux and the normal of the substrate surface. Right: Cross sectional SEM images of structures grown by e-beam evaporation for the deposition angles 0°, 30°, 50°, 70°.

Experimental results show a porous and columnar growth, which is illustrated by the SEM images in Fig. 7. Spectral photometric transmission measurements are performed and evaluated using the software OptiLayer. These experiments deliver an increasing anisotropy for larger deposition angles, which is plotted in Fig. 8. Obviously, the columnar growth seems to be more prominent for higher deposition angles. This impression is also supported by the more pronounced columnar structure, displayed by the SEM images for large glancing incidence angles, while for small angles the structure is porous with no clearly resolvable columns.
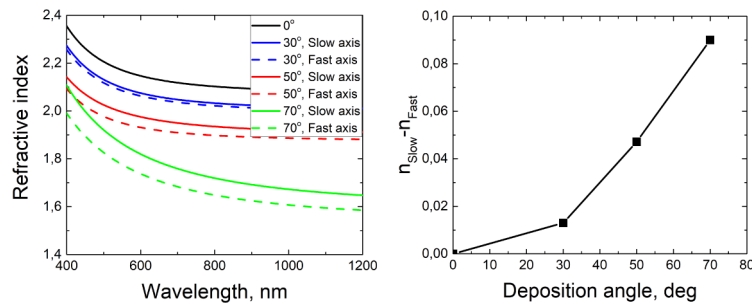
**Fig. 8.** Left: Measured refractive indices for different polarization states of the experimentally grown structures shown in Fig. 7. Right: The anisotropy dependent on the deposition angle. The error for the determination of $\Delta n$ can be assumed to range between 0.01 to 0.02.

## 6.   Structures grown with parameters for a DC magnetron sputtering plant

In this section the full simulation of the Mantis-coater is presented. The simulations allow revealing the influence of real growth conditions on the film properties. The Mantis coater is a lab coater which uses two DC magnetrons. Because of a relatively large distance between the magnetrons and the substrates as well as the gas pressure, the atoms in the incident fluxes are extensively, but not fully, thermalized [2]. The structures grown in accordance with the two substrate positions 22 and 23 (see Fig. 2), are shown in Figs. 9 and 10 as simulated structures and experimental SEM images. For the substrate position 22 with effectively normal incidence (Fig. 9), both methods, MD and kMC, return dense structures with no anisotropy. In contrast, the structures grown at the substrate position 23 (GLAD) reveal columnar growth (Fig. 10). The fill factors for the kMC structures are 80% for the position 22 and 66% for position 23, which fits to the values for discrete GLAD angles. The MD structures are grown with slightly different initial conditions; the substrate footprint is $28 \times 8 nm^2$, here. With this adjustment one dimension is increased by a factor of four compared to the structures presented above and now nearly coincides with the substrate size of the kMC coatings for one dimension. The main differences between the GLAD MD and kMC structures are the free space between the columns and the density of the columns itself, which are higher for the MD structure. The mean density of the MD structure for position 22 is 4.20 g/cm$^3$ (4.24 g/cm$^3$ without pores) and for position 23 a mean density of 2.88 g/cm$^3$ (4.21 g/cm$^3$ without pores) is obtained. Therefore the fill factor for position 23 (68%) fits well to the kMC structure, while for position 22 the MD gives a value of nearly 100%, which is much higher than the result obtained by kMC. Corresponding to the nearly unchanged density values of the pore-excluded structure, the radial distribution function (RDF) for both configurations show no difference (Fig. 11). That means, that the atomic configuration is left completely unchanged. For position 23 the slanting angle of the MD structure is significantly larger compared with the kMC value (see Table 4). For the viewing plane, where the tilt angle is in the direction towards the viewer, also columnar features are observable. The main components of the refractive index ellipsoid are $n_{a,b,c}$=(1.76, 1.85, 1.97) for the MD structure and $n_{a,b,c}$=(1.80, 1.81, 1.89) for the kMC structure, respectively.
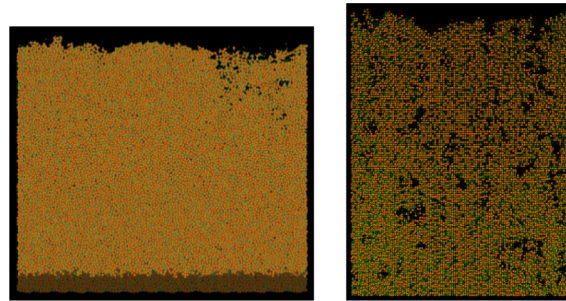
**Fig. 9.** Structures grown with parameters of a DC magnetron sputter plant (Mantis). The structures are grown with effectively normal incidence (position 22). Left MD and right kMC, both structures are compact.
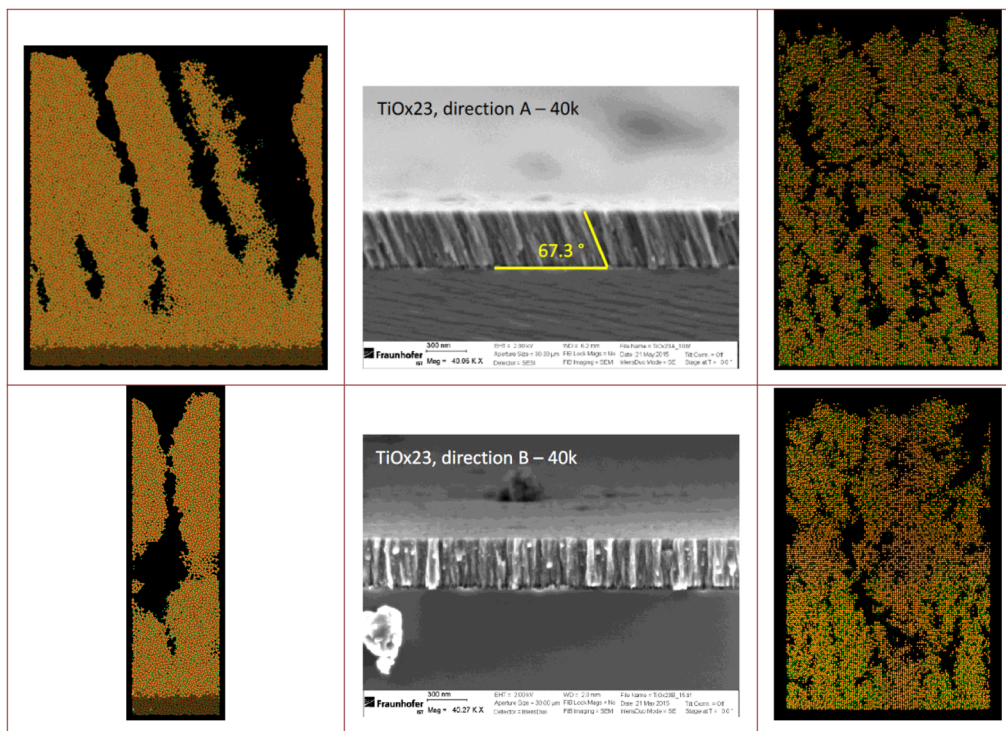


**Fig. 10.** Structures grown with parameters of a DC magnetron sputtering plant (Mantis). The structures are grown with the GLAD configuration (position 23) and show the column angle in the top row. For the bottom row the view direction is rotated by 90°, the columnar growth can be still viewed, however the tilt is in the direction of the viewing plane here (Left: MD with 500k atoms, Right: kMC with 1 Mio. atoms). SEM images of an experimental coating corresponding to the simulations is shown in the middle.
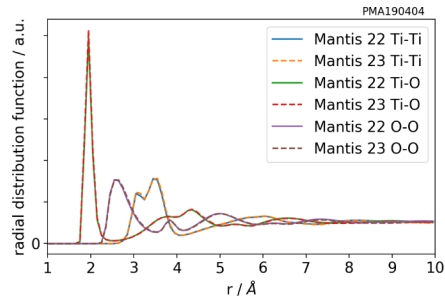
**Fig. 11.** Radial distribution functions (RDF) of the different atomic species for the MD simulated structures shown in Fig. 9 and 10. No change of the RDF can be observed, which means that the density of the columns correspond well to the density of bulk material.

**Table 4. Comparison of the refractive indices obtained by both simulation methods and from experimental samples. While the columnar tilt is well reproduced by both methods, the birefringence is only meaningfully described by MD, while the fill factor of the kMC fits better to the absolute indices of refraction.**

| $\theta$ | | molecular dynamics (MD) | kinetic Monte Carlo (kMC) | experimental coatings (at 600nm) |
|---|---|---|---|---|
| 0° | $n_s$ | 1.843 | 2.082 | 2.09 |
| | $n_p$ | 1.820 | 2.078 | 2.09 |
| | $\Delta n$ | 0.023 | 0.004 | 0 |
| | $\sigma$ | 1° | 4° | 0° |
| 30° | $n_s$ | 1.859 | 2.015 | 2.07 |
| | $n_p$ | 1.811 | 2.008 | 2.06 |
| | $\Delta n$ | 0.048 | 0.007 | 0.01 |
| | $\sigma$ | 15° | 5° | 10° |
| 50° | $n_s$ | 1.736 | 1.936 | 1.97 |
| | $n_p$ | 1.690 | 1.928 | 1.93 |
| | $\Delta n$ | 0.046 | 0.008 | 0.04 |
| | $\sigma$ | 24° | 24° | 22° |
| 70° | $n_s$ | 1.655 | 1.733 | 1.82 |
| | $n_p$ | 1.589 | 1.761 | 1.74 |
| | $\Delta n$ | 0.066 | −0.028 | 0.08 |
| | $\sigma$ | 51° | 44° | 32° |
| Mantis23 | $\sigma$ | 18° | 15° | 23° |

## 7.　Comparison of virtual materials generated by the MD and kMC methods with experimentally grown coatings

Both simulation techniques as well as the experimentally grown coatings show a clear inclination of the columnar structure, which increases for larger deposition angles. For a detailed comparison, the birefringence $\Delta n$ caused by the anisotropic structure is calculated for the simulations. The difference in index of refraction $\Delta n$ gives values that are in the order of $10^{-3}$ up to $10^{-1}$. The values obtain by the MD simulations are comparable to the experimental findings, while the kMC cannot reproduce them for large GLAD angles. However, for the systematic investigation with discrete deposition angles, the fill factors and therefore the absolute values of the indices of refraction of the kMC seems to fit well to the experiment. The estimate of the stochastic variation error due to small lateral structure sizes are prominent for the MD structures, which is about 0.02 (for 0° deposition angle), however in this range the values for the other deposition angles coincides with the experimentally obtained values. For a deposition angle of 50° the best coincidence for the birefringence is obtained. For normal and nearly normal incidence angles, the lateral larger structures of the kMC result in a lower variance compared to MD, and also well comparable values of the birefringence with the experiment. The columnar tilting angles show a good agreement between both methods and the experiment, although for 70° deposition both, MD and kMC, overestimate the columnar tilt. Also annealing effects, which are not handled in the simulations could play a non-negligible role here. The good agreement between the slanting angle of the MD structures with the empirical tangent rule indicates that here the simulation with only one discrete deposition angle does not fully describe the e-beam process. For 70°, the kMC even indicates a change of the fast and slow axis, which however does not coincide with the MD and experimental results. The inclination angle for the simulation of the Mantis-coater shows a satisfactory agreement between the MD and kMC structures and the experiment.

## 8.　Conclusion

The paper presents an algorithm for an evaluation of atomistic structures in view of anisotropic optical properties. This is demonstrated for structures generated by two different simulation methods, MD and kMC, for simple coating conditions in the Virtual Coater framework. The results are compared to experimental findings. Additionally the results for more realistic coating conditions with energetic and angular distributions are shown and compared with experiments. Because the MD models the structure growth with real atomic movement, while the kMC is based on probability and stochastic atomic placement, the MD promises a better description of the structures. However, the kMC is much faster compared with MD and therefore allows simulating much larger structures. The MD results show in sum a better agreement with the experimental values; however the larger structures that can be obtained by the kMC indicate advantages for small deposition angles and the fill factors. The thickness in growth direction seems to be sufficient for both methods, although the simulated thickness is only in the range of 10% compared with the experimental ones. That is also because influencing effects of the surface or the substrate regions are excluded in the analysis. In sum, the application of the numerical investigation of optical anisotropy establishes an extension of the Virtual Coater concept and shows the mutual advantages and disadvantages of two methods for the atomistic thin film growth.

## Acknowledgments

## References

1. M. Turowski, M. Jupé, T. Melzig, P. Moskovkin, A. Daniel, A. Pflug, S. Lucas, and D. Ristau, "Practice-oriented optical thin film growth simulation via multiple scale approach," Thin Solid Films **592**, 240–247 (2015).
2. R. Tonneau, P. Moskovkin, A. Pflug, and S. Lucas, "TiO$_x$ deposited by magnetron sputtering: a joint modelling and experimental study," J. Phys. D: Appl. Phys. **51**(19), 195202 (2018).
3. D. C. Rapaport, *The Art of Molecular Dynamics Simulation* (Cambridge University, 1996).
4. V. Georgieva, I. T. Todorov, and A. Bogaerts, "Molecular dynamics simulation of oxide thin film growth: Importance of the inter-atomic interaction potential," Chem. Phys. Lett. **485**(4-6), 315–319 (2010).
5. C. M. Gilmore and J. A. Sprague, *Molecular Dynamics Simulation of Thin Film Growth with Energetic Atoms* (Springer Netherlands, 2002), pp. 283–307.
6. A. F. Voter, "Introduction to the kinetic monte carlo method," in *Radiation Effects in Solids*, K. E. Sickafus, E. A. Kotomin, and B. P. Uberuaga, eds. (Springer Netherlands, 2007), pp. 1–23.
7. E. Haye, J. L. Colaux, P. Moskovkin, J.-J. Pireaux, and S. Lucas, "Wide range investigation of duty cycle and frequency effects on bipolar magnetron sputtering of chromium nitride," Surf. Coat. Technol. **350**, 84–94 (2018).
8. S. Lucas and P. Moskovkin, "Simulation at high temperature of atomic deposition, islands coalescence, ostwald and inverse ostwald ripening with a general simple kinetic monte carlo code," Thin Solid Films **518**(18), 5355–5361 (2010).
9. H. A. Macleod, *Thin-Film Optical Filters* (CRC, 2010).
10. M. Turowski, T. Amotchkina, H. Ehlers, M. Jupé, and D. Ristau, "Calculation of optical and electronic properties of modeled titanium dioxide films of different densities," Appl. Opt. **53**(4), A159–A168 (2014).
11. D. Schmidt and M. Schubert, "Anisotropic bruggeman effective medium approaches for slanted columnar thin films," J. Appl. Phys. **114**(8), 083510 (2013).
12. A. Mahdjoub and L. Zighed, "New designs for graded refractive index antireflection coatings," Thin Solid Films **478**(1-2), 299–304 (2005).
13. M. Born and E. Wolf, *Principles of Optics* (Cambridge University, 1999).
14. M. Luersen, R. Le Riche, and F. Guyon, "A constrained, globalized, and bounded nelder–mead method for engineering optimization," Struct. Multidiscip. Optim. **27**(1-2), 43–54 (2004).
15. S. Arseneau, *Junction Analysis: Representing Junctions through Asymmetric Tensor Diffusion* (VDM Verlag Dr. Müller e.K., 2008).
16. A. Pflug, M. Siemers, T. Melzig, D. Rademacher, T. Zickenrott, and M. Vergöhl, "Numerical optimization of baffles for sputtering optical precision filters," Surf. Coat. Technol. **241**, 45–49 (2014).
17. A. Pflug, M. Siemers, T. Melzig, L. Schäfer, and G. Bräuer, "Simulation of linear magnetron discharges in 2d and 3d," Surf. Coat. Technol. **260**, 411–416 (2014).
18. A. Pflug, M. Siemers, T. Melzig, M. Keunecke, L. Schäfer, and G. Bräuer, *Thin-Film Deposition Processes* (John Wiley & Sons, Ltd, 2016), chap. 2.7, pp. 157–189.
19. P. Hohenberg and W. Kohn, "Inhomogeneous electron gas," Phys. Rev. **136**(3B), B864–B871 (1964).
20. P. E. Blöchl, "Projector augmented-wave method," Phys. Rev. B **50**(24), 17953–17979 (1994).
21. J. P. Perdew, K. Burke, and M. Ernzerhof, "Generalized gradient approximation made simple," Phys. Rev. Lett. **77**(18), 3865–3868 (1996).
22. J. Heyd, G. E. Scuseria, and M. Ernzerhof, "Hybrid functionals based on a screened coulomb potential," J. Chem. Phys. **118**(18), 8207–8215 (2003).
23. M. Matsui and M. Akaogi, "Molecular dynamics simulation of the structural and physical properties of the four polymorphs of TiO$_2$," Mol. Simul. **6**(4-6), 239–244 (1991).
24. I. Todorov, W. Smith, K. Trachenko, and M. Dove, "Dl_poly_3: new dimensions in molecular dynamics simulations via massive parallelism," J. Mater. Chem. **16**(20), 1911–1918 (2006).
25. D. Wolf, P. Keblinski, S. R. Phillpot, and J. Eggebrecht, "Exact method for the simulation of coulombic systems by spherically truncated, pairwise r-1 summation," J. Chem. Phys. **110**(17), 8254–8282 (1999).
26. H. C. Andersen, "Molecular dynamics simulations at constant pressure and/or temperature," J. Chem. Phys. **72**(4), 2384–2393 (1980).
27. Université de Namur, "Nascam (nanoscale modeling), https://www.unamur.be/sciences/physique/larn/logiciels/nascam," (2018).
28. S. Blackwell, R. Smith, S. D. Kenny, and J. M. Walls, "Atomistic modelling of titania grown using pvd methods," *Photovoltaic Specialists Conference (PVSC), 2012 38th IEEE*, (IEEE, 2012), pp. 002306–002310.
29. A. Dirks and H. Leamy, "Columnar microstructure in vapor-deposited thin films," Thin Solid Films **47**(3), 219–233 (1977).
30. A. Zuber, H. Jänchen, and N. Kaiser, "Perpendicular-incidence photometric ellipsometry of biaxial anisotropic thin films," Appl. Opt. **35**(28), 5553–5556 (1996).